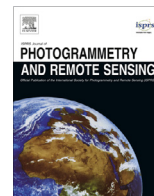


Contents lists available at [ScienceDirect](http://www.sciencedirect.com)

ISPRS Journal of Photogrammetry and Remote Sensing

journal homepage: www.elsevier.com/locate/isprsjprs

Sub-pixel mapping of remote sensing images based on radial basis function interpolation



Qunming Wang^{a,*}, Wenzhong Shi^{a,*}, Peter M. Atkinson^b

^a Department of Land Surveying and Geo-Informatics, The Hong Kong Polytechnic University, Kowloon, Hong Kong

^b Geography and Environment, University of Southampton, Highfield, Southampton SO17 1BJ, UK

ARTICLE INFO

Article history:

Received 28 September 2013

Received in revised form 19 February 2014

Accepted 25 February 2014

Available online 20 March 2014

Keywords:

Downscaling

Sub-pixel mapping (SPM)

Super-resolution mapping

Radial basis function (RBF) interpolation

Hard classification

ABSTRACT

In this paper, a new sub-pixel mapping (SPM) method based on radial basis function (RBF) interpolation is proposed for land cover mapping at the sub-pixel scale. The proposed method consists of sub-pixel soft class value estimation and subsequent class allocation for each sub-pixel. The sub-pixel soft class values are calculated by RBF interpolation. Taking the coarse proportion images as input, an interpolation model is built for each visited coarse pixel. First, the spatial relations between any sub-pixel within a visited coarse resolution pixel and its surrounding coarse resolution pixels are quantified by the basis function. Second, the coefficients indicating the contributions from neighboring coarse pixels are calculated. Finally, the basis function values are weighted by the coefficients to predict the sub-pixel soft class values. In the class allocation process, according to the class proportions and estimated soft class values, sub-pixels are allocated one of each available class in turn. Three remote sensing images were tested and the new method was compared to bilinear-, bicubic-, sub-pixel/pixel spatial attraction model- and Kriging-based SPM methods. Results show that the proposed RBF interpolation-based SPM is more accurate. Hence the proposed method provides an effective new option for SPM.

© 2014 International Society for Photogrammetry and Remote Sensing, Inc. (ISPRS) Published by Elsevier B.V. All rights reserved.

1. Introduction

Image classification, one of the most important techniques in remote sensing, is used widely to extract land cover information from remote sensing images. The inevitable mixed pixels (i.e., pixels that contain more than one land cover class) in remote sensing images have brought a great challenge for traditional hard classification-based land cover mapping. To solve this mixed pixel problem, soft classification has been developed to predict land cover proportions for land cover classes that have a spatial frequency higher than the interval between pixels (Bioucas-Dias et al., 2012; Foody, 2000; Heinz and Chang, 2001). Soft classifiers exploit the spectral information of remote sensing images (Wang and Wang, 2013), but fail to predict the spatial location of classes within mixed pixels. To address this issue, sub-pixel mapping (SPM) (Atkinson, 1997) has been developed, in which each mixed pixel is divided into multiple sub-pixels for which class labels are predicted. SPM, thus, transforms a soft classification into a finer resolution hard classification.

SPM is also termed super-resolution mapping (Atkinson, 2009) in the remote sensing literature. It is usually distinguished from super-resolution reconstruction or restitution in the fields of image and signal processing (Atkinson, 2009). For super-resolution reconstruction, the goal is to produce a finer spatial resolution image than that of the input coarse image by superimposing the input coarse image. Further, the output is usually a continuous variable. SPM refers to the prediction of a hard classified land cover map at a finer spatial resolution than the input such that the outputs is a set of categories (class labels). However, there are links between SPM and super-resolution reconstruction: for example, after super-resolution reconstruction of a remote sensing image in units of reflectance, the finer spatial resolution image could then be classified by a hard classifier to achieve SPM (Li et al., 2009).

SPM is often performed based on maximizing spatial dependence with the assumption that the land cover is spatially dependent both within and between pixels. Over the past decades, SPM has gained increasing attention in remote sensing and various SPM algorithms have been developed. As the post-processing of a soft classification, some SPM algorithms involve iterative optimization. Specifically, a fine spatial resolution land cover map is initialized first. Guided by a certain objective with the constraint from

* Corresponding authors. Tel.: +852 2766 5975.

E-mail addresses: wqm11111@126.com (Q. Wang), lszwzshi@polyu.edu.hk (W. Shi), P.M.Atkinson@soton.ac.uk (P.M. Atkinson).

class proportions (i.e., outputs of soft classification), the initialized fine spatial resolution map is optimized to obtain the SPM result (Atkinson, 2005; Mertens et al., 2003; Makido et al., 2007; Villa et al., 2011; Wang et al., 2012). The optimization process requires several iterations to approach a satisfactory result and often artificial intelligence algorithms are applied to solve the relevant models, such as genetic algorithms (Mertens et al., 2003), simulating annealing (Makido et al., 2007; Villa et al., 2011), Hopfield neural network (Tatem et al., 2001; Muad and Foody, 2012a; Nguyen et al., 2005) and particle swarm optimization (Wang et al., 2012). Much time is always needed in the optimization process.

Another type of SPM algorithm, namely, the soft-then-hard SPM (STHSPM) algorithm (Wang et al., 2014a), involves two steps: sub-pixel sharpening and class allocation. Sub-pixel sharpening is undertaken to obtain the soft class value (between 0 and 1) for sub-pixels while class allocation is used to allocate hard class labels (0 or 1) for sub-pixels according to the estimated soft class values and constraints from the class proportions. Commonly used STHSPM algorithms include sub-pixel/pixel spatial attraction model (SPSAM) (Mertens et al., 2006), back-propagation neural network (Nigussie et al., 2011), Kriging (Verhoeye and Wulf, 2002) and Indicator CoKriging (Boucher and Kyriakidis, 2006; Jin et al., 2012; Wang et al., 2014b).

SPM can also be performed by one-stage methods that instead of taking a soft classified image as input (i.e., two stages of soft classifier and SPM), take the raw image in units of reflectance as input (Kasetkasem et al., 2005; Tolpekin and Stein, 2009; Ardila et al., 2011; Ling et al., 2012a) (thus, one stage). In these methods, spectral and spatial information are considered simultaneously. In addition, Foody et al. (2005) and Su et al. (2012) present a contouring method for SPM that draws the boundaries of classes running through the coarse pixels. This method is more suitable for large objects.

For the STHSPM algorithm, a solution can be achieved without iterations. Note the iterations in the training process in a back-propagation neural network are not considered, since the training process is always off-line. Hence, SPM can be realized quickly for the STHSPM algorithm. Thus, the objective of this paper was to develop further this type of algorithm.

The outputs of sub-pixel sharpening in the STHSPM algorithm are continuous values between 0 and 1, which indicate the probabilities of class occurrence at each sub-pixel. Actually, the task of sub-pixel sharpening can be viewed as downscaling the coarse spatial resolution proportion images to the target spatial resolution. This task can also be accomplished by super-resolution reconstruction when the proportion images are taken as input. It would be worth employing super-resolution reconstruction algorithms for the purpose of sub-pixel sharpening.

In this paper, for the first time, a SPM algorithm based on radial basis function (RBF) interpolation is proposed. Interpolation-based super-resolution algorithms have been used widely for image downscaling. They can process a single coarse spatial resolution image by exploiting the spatial information encapsulated in the input image. As a powerful tool for modeling a non-linear function from given input–output data, RBFs have attracted considerable attention in many areas, such as neural networks (González et al., 2003), solution of differential equations (Pollandt, 1997), scattered data interpolation (Torres and Barba, 2009), and structure optimization (Wang et al., 2007). A detailed overview of RBFs and their applications can be found in Buhmann (2003). RBFs are known widely as a versatile tool for image interpolation (Lee and Yoon, 2010; Magoules et al., 2007). In RBF-based image interpolation, a system of equations is solved to obtain the RBF coefficients that characterize the input–output mapping (Fuji et al., 2012). The matrices described by the basis function are always uniquely solvable for most stencils in two-dimensional space (Lee and Yoon,

2010). RBF interpolation has been shown to be a highly accurate super-resolution reconstruction algorithm (Lee and Yoon, 2010; Magoules et al., 2007), both theoretically and practically, and has gained a wide range of successful applications, including medical image processing (Carr et al., 1997) and computer graphics (Carr et al., 2001). These properties and advantages of RBFs allow their application in SPM. In the proposed RBF interpolation-based SPM, the coarse proportion images are used as input and soft class values at sub-pixels are estimated by RBF interpolation. Conditional upon the original class proportions constraint that fixes the number of sub-pixels allocated to each class per pixel, the estimated soft class values are then hardened to generate a hard classified land cover map at the sub-pixel scale.

The proposed RBF interpolation-based SPM belongs to the aforementioned STHSPM algorithm. Similar to SPSAM-, back-propagation neural network-, Kriging- and Indicator CoKriging-based SPM, the proposed algorithm is a non-iterative method, and the uncertainty introduced by random initialization and stochastic processes involved in the iterations of the first type of SPM can also be avoided. On the other hand, compared to back-propagation neural network- and Indicator CoKriging-based SPM, the proposed SPM algorithm has the advantage of not relying on any prior model of land cover spatial structure. The RBF interpolation-based SPM is performed by exploiting fully the spatial information in the input proportion images.

The remainder of this paper is organized as follows. Section 2 describes the SPM problem. Section 3 gives details of the proposed SPM method, including sub-pixel soft class value prediction and hard class allocation. Experimental results are provided in Section 4 and discussed in detail in Section 5. The conclusions are drawn in Section 6.

2. The SPM problem

The SPM approach in this paper represents a post-processing step following soft classification. In SPM, each mixed pixel is divided into multiple sub-pixels and then their class labels are predicted. The coarse proportion data and the zoom factor are used to calculate the number of sub-pixels for each class. The details are given below.

2.1. Calculation of the number of sub-pixels for each class

Suppose S is the zoom factor (i.e., each coarse pixel is divided into $S \times S$ sub-pixels), P_j ($j = 1, 2, \dots, M$, M is the number of pixels in the coarse image) is a coarse pixel and $F_k(P_j)$ is the coarse proportion of the k -th ($k = 1, 2, \dots, K$, K is the number of classes) class for pixel P_j . Considering the physical meaning, the coarse proportions estimated by soft classification (e.g., spectral unmixing (Bioucas-Dias et al., 2012)) usually meet the abundance sum-to-one constraint and the abundance non-negativity constraint, i.e.,

$$\sum_{k=1}^K F_k(P_j) = 1, \quad j = 1, 2, \dots, M \quad (1)$$

$$F_k(P_j) \geq 0, \quad k = 1, 2, \dots, K; \quad j = 1, 2, \dots, M$$

For a particular pixel, say P_j , the number of sub-pixels for the k -th class, $E_k(P_j)$, is calculated by

$$E_k(P_j) = \text{round}(F_k(P_j)S^2) \quad (2)$$

where $\text{round}(\cdot)$ is a function that takes the integer nearest to \cdot . The sum of the numbers of sub-pixels for all K classes are S^2 .

2.2. Prediction of class labels for sub-pixels

Let p_i ($i = 1, 2, \dots, MS^2$) be a sub-pixel and $B_k(p_i)$ be the binary class indicator for the k -th class at sub-pixel p_i

$$B_k(p_i) = \begin{cases} 1 & \text{if sub-pixel } p_i \text{ belongs to class } k \\ 0, & \text{otherwise} \end{cases} \quad (3)$$

In the SPM result, each sub-pixel should be assigned to only one class and the number of sub-pixels for each class should be consistent with the coarse proportion data, which are described as

$$\sum_{k=1}^K B_k(p_{j,i}) = 1, \quad i = 1, 2, \dots, S^2; \quad j = 1, 2, \dots, M \quad (4)$$

$$\sum_{i=1}^{S^2} B_k(p_{j,i}) = E_k(P_j), \quad k = 1, 2, \dots, K; \quad j = 1, 2, \dots, M$$

where sub-pixel $p_{j,i}$ falls within coarse pixel P_j .

The critical task of SPM is to obtain the binary class indicators for all classes at each sub-pixel. In this paper they are predicted according to the soft class values at each sub-pixel estimated by RBF interpolation. The principle is introduced in the following section.

3. RBF interpolation-based SPM

3.1. Estimation of soft class values at the sub-pixel scale using RBF interpolation

The RBF interpolation discussed in this paper involves area-to-point prediction (Atkinson, 2013), which refers to the super-resolution of continua (proportion images in this paper) through interpolation and is different from the common interpolation task of predicting between sparsely distributed points (Buhmann, 2003). In area-to-point prediction, the input variable (at a coarse resolution) is the same as the output variable (at a fine resolution) and both are generally continuous variables (Atkinson, 2013).

Let $F_k(p_i)$ be the soft class value for the k -th class at sub-pixel p_i . The task of RBF interpolation is to predict $\{F_k(p_i) | i = 1, 2, \dots, MS^2, k = 1, 2, \dots, K\}$ at the target fine spatial resolution. The variables in this section that have been mentioned in Section 2 have the same meaning as in Section 2.

In RBF interpolation, the soft class value $F_k(p_i)$ is predicted by

$$F_k(p_i) = \sum_{n=1}^N \lambda_k(P_n) \phi(P_n, p_i) \quad (5)$$

where N is the number of observed coarse pixels that are usually in a local window, $\lambda_k(P_n)$ is the coefficient of the k -th class for coarse pixel P_n , and $\phi(P_n, p_i)$ is a basis function that describes the spatial relation between sub-pixel p_i and coarse pixel P_n . The estimated soft class value is a weighted linear combination of N values calculated by the basis function. Correspondingly, two terms are needed for RBF interpolation: basis function values and their coefficients.

3.1.1. Basis function values

Suppose $d(P_n, p_i)$ is the Euclidean distance between the geometric centers of pixel P_n and sub-pixel p_i . A commonly used basis function in RBF interpolation is the Gaussian function (Lee and Yoon, 2010)

$$\phi(P_n, p_i) = e^{-d^2(P_n, p_i)/a^2} \quad (6)$$

in which a is a parameter. The larger the distance, the smaller the basis function value (i.e., the weaker the spatial relation). An example is provided in Fig. 1 to illustrate the calculation of $d(P_n, p_i)$. Suppose there are N observed coarse pixels in a $N_0 \times N_0$ ($N_0 = 3$ in Fig. 1)

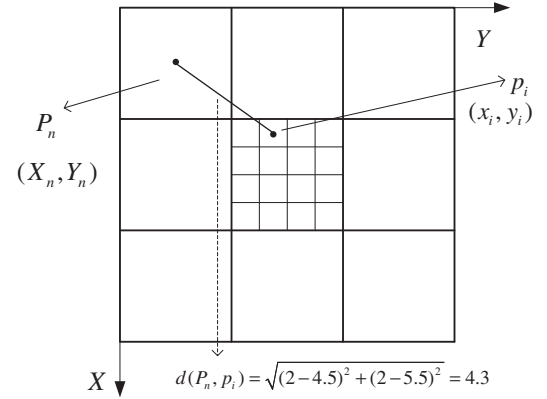


Fig. 1. Illustration of distance calculation between pixel P_n and sub-pixel p_i .

local window and each coarse pixel is divided into S by S sub-pixels ($S = 4$ in Fig. 1); coarse pixel P_n is in the R_n -th row and C_n -th ($R_n, C_n = 1, 2, \dots, N_0$) column in the local window; sub-pixel p_i is in the r_i -th row and c_i -th ($r_i, c_i = 1, 2, \dots, S$) column in the coarse pixel that it falls within. The coordinates of P_n and p_i , denoted as (X_n, Y_n) and (x_i, y_i) , are calculated as

$$\begin{aligned} X_n &= (R_n - 0.5)S \\ Y_n &= (C_n - 0.5)S \\ x_i &= 0.5(N_0 - 1)S + r_i - 0.5 \\ y_i &= 0.5(N_0 - 1)S + c_i - 0.5 \end{aligned} \quad (7)$$

The distance between them is

$$d(P_n, p_i) = \sqrt{(X_n - x_i)^2 + (Y_n - y_i)^2} \quad (8)$$

3.1.2. Coefficients

With respect to the coefficient $\lambda_k(P_n)$, it indicates the contribution from neighboring coarse pixel P_n . The coefficients are determined by exploiting the available information in the input proportion images. For each observed coarse pixel P_j , (9) holds

$$F_k(P_j) = \sum_{n=1}^N \lambda_k(P_n) \phi(P_n, P_j), \quad j = 1, 2, \dots, N \quad (9)$$

where $\phi(P_n, P_j)$ is the quantified spatial relation between pixel P_n and pixel P_j . It is calculated in the same way as that in (6). Combining all N equations, we can compute the coefficient sets $\lambda_k = [\lambda_k(P_1), \lambda_k(P_2), \dots, \lambda_k(P_N)]^T$ by solving the following equation

$$\Phi \lambda_k = \mathbf{F}_k \quad (10)$$

in which

$$\mathbf{F}_k = [F_k(P_1), F_k(P_2), \dots, F_k(P_N)]^T \quad (11)$$

The superscript T denotes a matrix transposition, and

$$\Phi = \begin{bmatrix} \phi(P_1, P_1) & \phi(P_2, P_1) & \dots & \phi(P_N, P_1) \\ \phi(P_1, P_2) & \phi(P_2, P_2) & \dots & \phi(P_N, P_2) \\ \dots & \dots & \dots & \dots \\ \phi(P_1, P_N) & \phi(P_2, P_N) & \dots & \phi(P_N, P_N) \end{bmatrix} \quad (12)$$

As can be seen from (12), Φ is a matrix with $N \times N$ elements and the computing complexity in (10) scales quadratically with N . Moreover, for each mixed pixel, (10) is computed once and hence in the whole image the computation time of (10) is equal to the number of mixed pixels, which is always very large. Last but not least, the spatial dependence decreases when the distance between

pixels increases. For these reasons, it is unrealistic to use a large number of observed coarse pixels in RBF interpolation-based SPM, and a neighborhood window is used for each sub-pixel.

The soft class value prediction in RBF interpolation is different from that in the existing SPSAM-based SPM method. More precisely, in the latter, the soft class value is a weighted linear combination of the class proportions in neighboring coarse pixels, and the weights are quantified straightforwardly by the distances. In RBF interpolation, however, the soft class value is a weighted linear combination of the basis function values. The weights in RBF interpolation (i.e., coefficient sets λ_k) are calculated by using not only proportions in neighboring coarse pixels, but also the available information about spatial dependence in the neighborhood window: When calculating the coefficients, the spatial autocorrelation between coarse pixels in the neighborhood window is accounted for, as can be found from (10) and (12). This is the unique advantage of RBF interpolation.

The pseudocode of RBF interpolation is given below, where $p_{j,i}$ denotes any sub-pixel that falls within coarse pixel P_j .

RBF interpolation for prediction of soft class values at the sub-pixel scale

Inputs: $\{F_k(P_j) | j = 1, 2, \dots, M; k = 1, 2, \dots, K\}$ and S .

for $k = 1: K$
 for $j = 1: M$
 Select a neighborhood window with N coarse pixels
 Computation of coefficient vector λ_k using (10)
 for $i = 1: S^2$
 Calculation of N basis function values using (6)
 Estimation of $F_k(p_{j,i})$ using (5)
 end
 end
 end

Outputs: $\{F_k(p_{j,i}) | i = 1, \dots, S^2; j = 1, \dots, M; k = 1, \dots, K\}$.

3.2. Estimation of hard class values at the sub-pixel scale by class allocation

SPM is essentially an algorithm for hard classification at the sub-pixel scale and its outputs are hard attribute values. After the $\{F_k(p_i) | i = 1, 2, \dots, MS^2; k = 1, 2, \dots, K\}$ are estimated by RBF interpolation, with the constraints in (4), they are used to predict hard class labels $\{B_k(p_i) | i = 1, 2, \dots, MS^2; k = 1, 2, \dots, K\}$, as defined in (3).

In this paper, classes are allocated to sub-pixels class-by-class, using a class allocation method presented in our previous work (Wang et al., 2014a). Specifically, a visiting order of all classes is defined first and the number of sub-pixels for each class is calculated by (2). According to this order, the sub-pixels for the visited class are selected by comparing the soft class values for this class: The sub-pixel with the largest soft class value is selected before those with smaller soft class values and the process for this class is repeated until all sub-pixels for it are completely exhausted. The remaining sub-pixels are then used for the allocation of the next class. The whole class allocation process is terminated when each sub-pixel is allocated to a class. This method is fast and reproduces exactly the coarse proportion data. It is processed on each probability map at fine spatial resolution in turn, which encapsulates intra-class spatial correlation. With this class allocation method, therefore, autocorrelation for each class at the sub-pixel scale can be maximized. In the class allocation, different visiting orders of classes lead to different SPM results and the order needs

to be specified reasonably. According to Wang et al. (2014a), the visiting order of all classes can be specified by comparing the Moran's I (Makido et al., 2007) of all K classes at the pixel scale. Moran's I is an index of intra-class spatial correlation. The larger the index, the larger the autocorrelation. For each class, the index is estimated by using directly the proportion image of the given class. The K indices are ranked in decreasing order and the classes with larger indices are visited first. The pseudocode of the class allocation method is displayed below (Wang et al., 2014a).

Class allocation for RBF interpolation-based SPM

Inputs: $\{F_k(p_{j,i}) | i = 1, \dots, S^2; j = 1, \dots, M; k = 1, \dots, K\}$;
 $\{E_k(P_j) | j = 1, 2, \dots, M; k = 1, 2, \dots, K\}$.

Define a visiting order of K classes: k_1, k_2, \dots, k_K

for $r = 1: K$

for $j = 1: M$

Rank sequence $F_{k_r}(p_{j,1}), F_{k_r}(p_{j,2}), \dots, F_{k_r}(p_{j,S^2})$ in a decreasing order: $F_{k_r}(p_{j,D_1}), F_{k_r}(p_{j,D_2}), \dots, F_{k_r}(p_{j,D_{S^2}})$

for $i = 1: E_{k_r}(P_j)$

$B_{k_r}(p_{j,D_i}) = 1$

end

for $i = E_{k_r}(P_j) + 1: S^2$

$B_{k_r}(p_{j,D_i}) = 0$

end

end

Sub-pixels that have been allocated to class k_r are not considered for the remaining classes

end

Outputs: $\{B_k(p_{j,i}) | i = 1, \dots, S^2; j = 1, \dots, M; k = 1, \dots, K\}$.

The flowchart of the proposed SPM method is shown in Fig. 2, where a map in Tatem (2002) is used for illustration. The map covers an area in Bath, UK, and has 360 by 360 pixels with a pixel size of 0.6 m by 0.6 m.

4. Experiments

4.1. Experimental setup

Three experiments were carried out for validation of the proposed RBF interpolation-based SPM method. The proposed method was compared to SPSAM and Kriging-based SPM methods in the experiments. The other two STHSPM algorithms, back-propagation neural network and Indicator CoKriging, were not compared in experiments because they need prior spatial structure information. As suggested by the principle of the proposed SPM method, other image interpolation methods are also expected to have potential in SPM. Hence, two well-known image interpolation algorithms, bilinear and bicubic, were also applied to SPM for comparison with the RBF interpolation-based SPM method. Specifically, bilinear and bicubic interpolation were used to predict the soft class values at each sub-pixel, and then class allocation method introduced in Section 3.2 was employed for hard class value prediction (Wang and Shi, 2014). In total, five SPM methods were tested: bilinear-, bicubic-, SPSAM-, Kriging- and RBF-based SPM algorithms. The accuracy of SPM was evaluated quantitatively by the overall accuracy in terms of the percentage of correctly classified pixels (PCC). For the proposed SPM method, the parameter a in the basis function was set to 10 and the window size N was set to 5. All experiments were run on an Intel Core 2 Processor (1.800-GHz Duo central

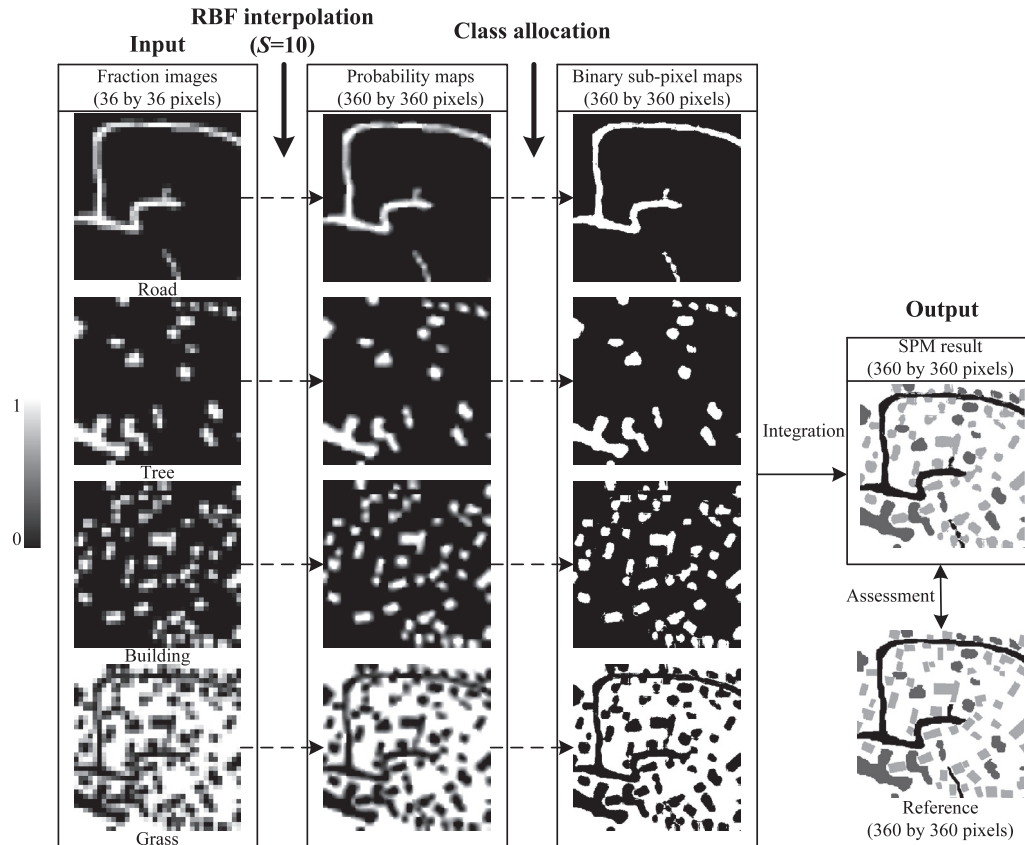


Fig. 2. Flowchart of the proposed RBF interpolation-based SPM.

processing unit, 2.00-GB random access memory) with MATLAB 7.1 version.

In the first experiment, three synthetic coarse spatial resolution images were used for testing, to avoid the errors from soft classification and solely concentrate on the performance of the proposed SPM method. More specifically, land cover maps were obtained by hard classification of the remote sensing images and these maps were used as reference. The reference maps were then degraded by an S by S mean filter (i.e., every S by S fine pixels were degraded to a coarse pixel) to generate the coarse proportion images. Finally, SPM methods were implemented to yield land cover maps with the same spatial resolution as the reference maps, by zooming in the proportion images with a scale factor S . Using synthetic coarse images, the input

proportions contain no uncertainty and the reference land cover maps are completely reliable for accuracy assessment.

In the second experiment, a hyperspectral image in the first experiment was degraded band by band with two scales to generate two coarse spatial resolution hyperspectral images. Soft classification was then performed to yield proportion images and SPM methods were implemented subsequently. Similarly to the first experiment, the hard classification result of the fine spatial resolution hyperspectral image was used as reference for SPM evaluation. This experiment was used to consider the inherent uncertainty in soft classification (Atkinson, 2009).

In the last experiment, the five SPM methods were tested with multiple zoom factors, in order to further validate the effectiveness and advantages of the proposed SPM method and also test the influence of S on its performance. Moreover, the influence of parameter a in the basis function (6) and window size N were tested for the proposed SPM method.

4.2. Data description

Three images were used in the experiments in all, including an aerial image and two hyperspectral images. Detailed information on the three datasets is now provided.

4.2.1. The Aerial image

An aerial image in Tatem (2002) was used for testing. The image covers an area in the city of Bristol, UK and for the purposes of this experiment can be considered to contain five land cover classes: grass, road, river, soil and tree. The image has 170 by 170 pixels with a pixel size of 4 m by 4 m. Fig. 3a shows the image while Fig. 3b shows the reference land cover map. The land cover pattern

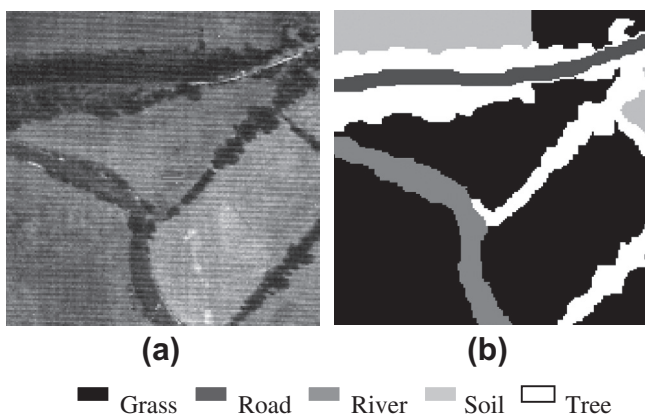


Fig. 3. (a) The aerial image. (b) The reference land cover map.

in Fig. 3b is relatively simple and the five classes appear mainly as large objects.

4.2.2. The Reflective Optics System Imaging Spectrometer (ROSIS) dataset

This dataset was acquired by the ROSIS sensor during a flight campaign over Pavia, northern Italy. The hyperspectral image has a spatial resolution of 1.3 m and 102 bands. A region with 400 by 400 pixels was studied, which covers six classes of interest: shadow, water, road, tree, grass and roof. The three-band color image (bands 102, 56, and 31 for RGB) is shown in Fig. 4a. The corresponding reference land cover map is shown in Fig. 4b, which was obtained with the tensor discriminative locality alignment-based classification of the hyperspectral data in Zhang et al. (2013).

4.2.3. The QuickBird dataset

The 0.61 m QuickBird image covers an area of the suburb of Xuzhou City, China, containing 480 by 480 pixels and three multi-spectral bands (RGB). The image was classified with an algorithm that first integrated spatial features of pixel shape feature set, grey level co-occurrence matrix and Gabor transform with spectral information and then used a support vector machine for classification. The generated land cover map contains seven classes: shadow, water, road, tree, grass, roof and bare soil. Fig. 5a shows the RGB image and Fig. 5b shows the hard classified land cover map. Through visual comparison, one can find that the land cover patterns in Figs. 4b and 5b are more complex than those in Fig. 3b.

4.3. Experiment 1 – Synthetic coarse images

The three maps in Figs. 3b, 4b, 5b were degraded with an 8 by 8 mean filter. Fig. 6 shows the produced proportion images. The sizes of the coarse spatial resolution images in the three lines for the three corresponding maps are 21 by 21, 50 by 50 and 60 by 60. As can be seen from the proportion images, the boundaries of classes are blurred, which necessitates SPM techniques. For SPM of the three coarse images in this experiment, the zoom factor was set to $S = 8$ to restore the fine spatial resolution images. The five SPM methods (i.e., bilinear, bicubic, SPSAM, Kriging and RBF-based SPM) were applied to the three groups of coarse proportion images. Table 1 gives the Moran's I estimated from the class proportion images and the specified visiting order of classes for class allocation process.

Figs. 7–9 display the SPM results for three images. Visual comparison of the five SPM results in each group in Figs. 7–9 reveals that the proposed method can be usefully applied to the SPM of

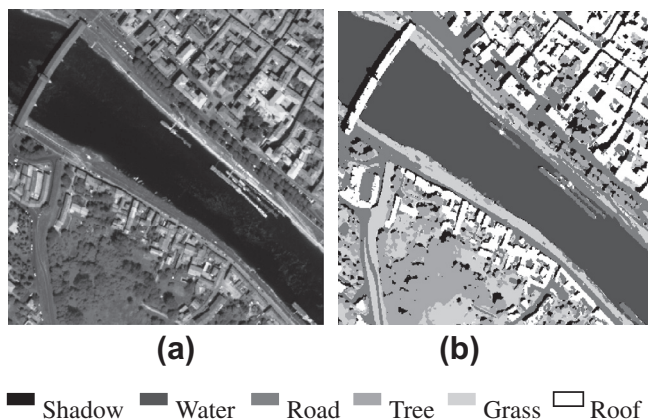


Fig. 4. (a) The three-band color image of the ROSIS hyperspectral dataset. (b) The reference land cover map.

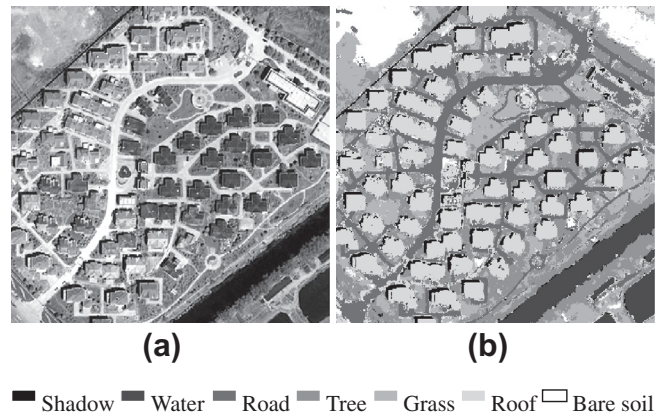


Fig. 5. (a) The QuickBird image. (b) The reference land cover map.

coarse images. Furthermore, the proposed method provides the most satisfactory SPM results among the five methods. Specifically, with respect to the results in Fig. 7a–e for the aerial image, the boundaries of classes are the smoothest in Fig. 7e, and it is the closest to the reference map in Fig. 3b. As an example, the boundaries of the road and tree classes in the top right of the image (marked by the pink rectangle in Fig. 7f) in the bilinear, bicubic and Kriging results are quite rough. For the SPSAM method, the restoration of the tree class in the same site is more satisfactory when compared to the bilinear, bicubic and Kriging methods, but still less acceptable than that of the proposed method. While examining Fig. 8a–d for the ROSIS image, one can see that there are many linear artifacts and the spatial continuity of each class is weak, especially in the bilinear and SPSAM results. Using the proposed SPM method, however, the predicted map in Fig. 8e has less linear artifacts and the distribution of classes is more continuous. This is particularly well illustrated by the results of mapping the roof and road classes (see the areas marked by the pink rectangles in Fig. 8f). Consistent with the results for the aerial and ROSIS images, for the QuickBird image, RBF result in Fig. 9e is found to have more continuous boundaries of classes than the other four maps in Fig. 9a–d.

Tables 2–4 list the classification accuracies of each class as well as the overall accuracy in terms of PCC for the SPM results of the three coarse images. To illustrate the gain of using SPM technique for land cover mapping, traditional pixel-level hard classification (HC) was performed, in which all sub-pixels within a coarse pixel are assigned to the dominated class. Note that the pure coarse pixels in Fig. 6 were not considered in the accuracy statistics because these pure pixels will only increase the accuracy without providing any useful information on the performance of the SPM methods (Mertens et al., 2003; Zhong and Zhang, 2012). Comparison of the PCC values of HC and the five SPM methods in Tables 2–4 reveals that SPM can produce obviously greater accuracy than HC method. For the aerial image, the accuracy gain of SPM over HC is around 15% and for the other two images, the gain is around 5%. As can be seen from Table 2, the Kriging method provides the greatest accuracy of classification for the river class. For the other four classes, the classification accuracy in the RBF result is the highest among the five SPM methods. The PCC of the RBF result reaches 92.63%, which is also higher than that of the other four SPM methods. In Table 3, the proposed RBF interpolation-based method achieves the greatest accuracy for all six classes in the ROSIS image. For example, the classification accuracy of the road class in the RBF result is 74.64%, which is 2.43%, 1.72%, 1.54% and 1.18% more than for the bilinear, bicubic, SPSAM and Kriging results; the classification accuracy of the roof class in the RBF result is 81.91%, which is greater by 1.53%, 1.04%, 1.15% and 0.86%, respectively. The

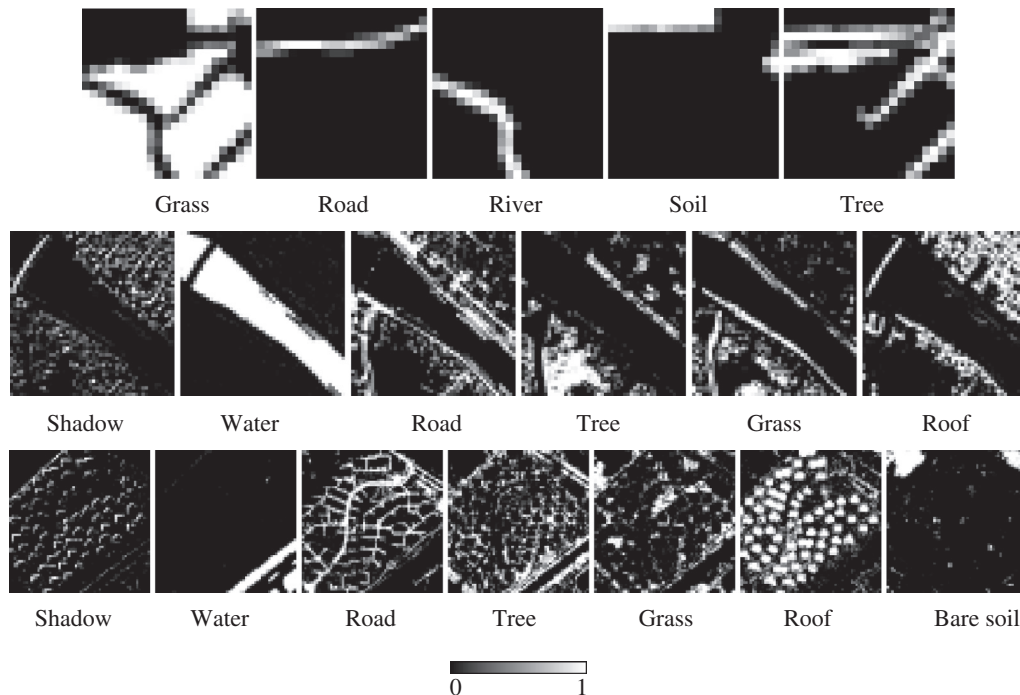


Fig. 6. Proportion images of the classes in the degraded land cover maps of three images. Line 1: Aerial image; Line 2: ROSIS image; Line 3: QuickBird image.

Table 1

Visiting order of classes for class allocation.

| | | | | | | | | |
|-----------------|-------------|--------|--------|--------|--------|--------|--------|-----------|
| Aerial image | Class | Grass | Road | River | Soil | Trees | | |
| | Moran's I | 0.7181 | 0.3244 | 0.6083 | 0.8042 | 0.5033 | | |
| | Order | 2 | 5 | 3 | 1 | 4 | | |
| ROSIS image | Class | Shadow | Water | Road | Tree | Grass | Roof | |
| | Moran's I | 0.3087 | 0.9212 | 0.5706 | 0.7427 | 0.5540 | 0.6449 | |
| | Order | 6 | 1 | 4 | 2 | 5 | 3 | |
| QuickBird image | Class | Shadow | Water | Road | Tree | Grass | Roof | Bare soil |
| | Moran's I | 0.2540 | 0.8505 | 0.4725 | 0.4728 | 0.5829 | 0.6044 | 0.8908 |
| | Order | 7 | 2 | 6 | 5 | 4 | 3 | 1 |

high accuracy for the proposed method may be attributed mainly to the fact that the predicted map has fewer linear artifacts and a more continuous distribution of classes, as mentioned in the above visual inspection for Fig. 8. Regarding the overall accuracy, the PCC of the proposed method is 74.89%, with gains of 1.99%, 1.34%, 1.55% and 1.03% over the bilinear, bicubic, SPSAM and Kriging methods. Focusing on Table 4, for the proposed method based on RBF interpolation, the classification of the roof class is less accurate than for the bicubic method, but the classification of the other six classes is the most accurate among the five SPM methods and the overall accuracy of the RBF method is the highest. More precisely, the SPSAM method has the lowest PCC, 71.88%, among the five SPM methods. For another three methods, bilinear, bicubic and Kriging, the PCC increased to 72.10%, 72.67% and 72.38%. However, their accuracies were still lower than that of the RBF method which produced a PCC of 73.24%.

4.4. Experiment 2-Degraded hyperspectral images

In this experiment, the ROSIS hyperspectral image used in the first experiment was degraded band by band with $S = 4$ and 8. In this way, two coarse hyperspectral images with spatial resolutions of 5 m and 10 m were produced. Prior to SPM, soft classification was essential to obtain the proportions of land cover classes within coarse pixels. Here, linear spectral mixture analysis (LSMA) (Heinz

and Chang, 2001) was employed for soft classification, appreciating its simple physical meaning and its convenience in application (Wang and Wang, 2013). The generated proportion images for six classes at $S = 8$ are shown in Fig. 10. Fig. 11a–e displays SPM results of the five methods for these coarse proportion images. The reference map in Fig. 4b was used for both visual and quantitative assessment of the five SPM methods, which has an overall accuracy of 96.42% and hence provides a useful reference data set.

It is worth noting that some scattering of pixels exists in the resulting maps (Fig. 11). For example, some pixels that should belong to the water class were classified as the road class. The reason for this phenomenon is that there were inherent errors in the outputs of LSMA and they were propagated to the SPM results (Ge, 2013). Similar to the results in the first experiment, the distribution of land cover classes in Fig. 11e is the closest to that in the reference map in Fig. 11f. As an instance, at the right bottom in Fig. 11a–d, some pixels near the water class should be of the road class, but were misclassified as the roof class. In the RBF result, however, these pixels were almost always correctly classified and the road class within it seems more continuous than in the other four

The quantitative assessment results for both $S = 4$ and $S = 8$ are listed in Table 5. Note that in this experiment all coarse pixels in Fig. 10 were included in the accuracy statistics, because errors in soft classification need to be considered. One can observe from

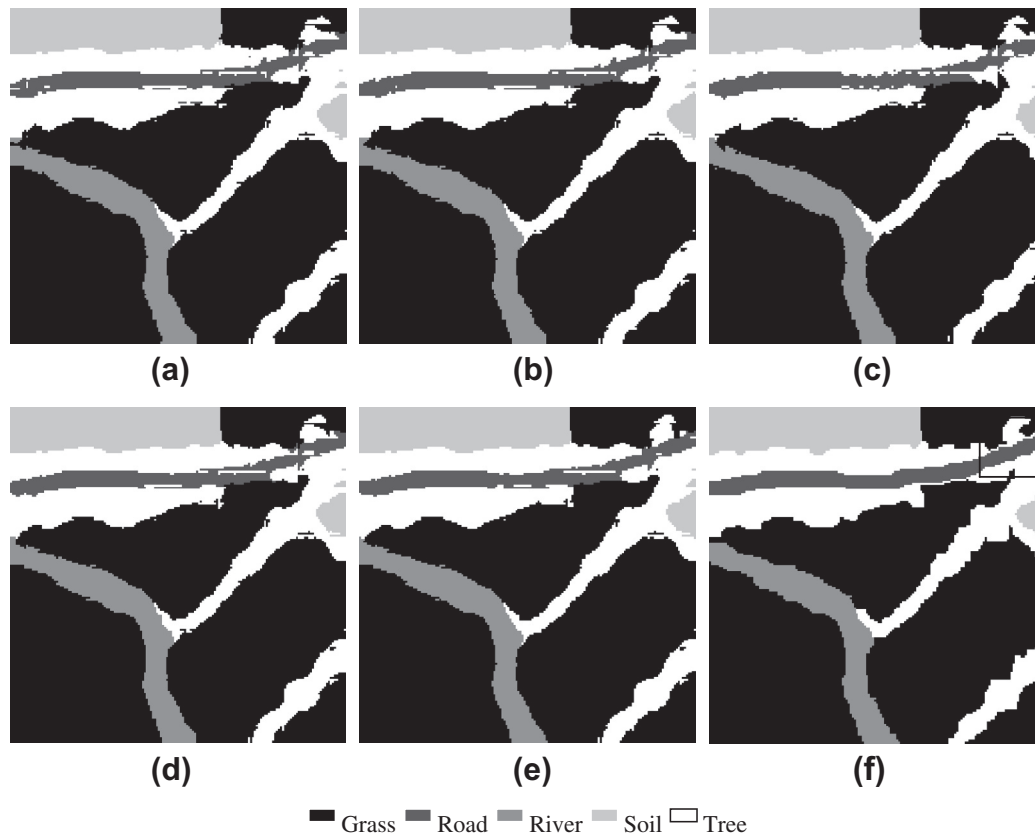


Fig. 7. SPM results of the five methods for the degraded land cover map of the aerial image ($S = 8$). (a) Bilinear. (b) Bicubic. (c) SPSAM. (d) Kriging. (e) RBF. (f) Reference with marked area.

the table that the bilinear method provides the lowest accuracy at both scales. Although bicubic and SPSAM methods can produce a more accurate SPM than the bilinear method, the PCC of them is still less than that of the Kriging method. For the proposed RBF method, it is able to achieve the highest accuracy for each class in nearly all cases. As for the overall accuracy, the RBF obtains a PCC of 75.08% at $S = 4$ and 70.45% at $S = 8$, both of which are the highest among the five methods.

4.5. Experiment 3 – Influences of parameter a in the basis function, zoom factor S and window size N

4.5.1. Influence of zoom factor

The five SPM methods were tested with different zoom scale factors using three groups of synthetic coarse images. The coarse images were produced by degrading the maps in Figs. 3b, 4b, and 5b with four different scales. In detail, the reference map in Fig. 3b was degraded with $S = 5, 8, 10$ and 15 while the reference maps in Figs. 4b and 5b were both degraded with $S = 4, 6, 8$ and 12. Fig. 12a–c exhibits the PCC (pure pixels were excluded for accuracy statistics) of the five SPM methods for three groups of coarse images. It is worth noting that as the scale increases, the accuracy of all five methods decreases. Precisely, the PCC of the five methods decreases by about 10% from $S = 5$ to $S = 15$ for the aerial image, 15% from $S = 4$ to $S = 12$ for the ROSIS image and 10% from $S = 4$ to $S = 12$ for the QuickBird image.

Table 6 summarizes the comparison of SPM accuracy between the five methods in Fig. 12. From the results for all 12 cases in the table, we can see that the SPSAM and bilinear methods are competent in SPM in general. As for the bicubic method, it outperforms both the SPSAM and bilinear methods. While comparing the

bicubic and Kriging methods, one can observe that the latter tends to provide more accurate SPM results. Focusing on the values in the last column, the proposed RBF method is found to be superior to the other four SPM methods in nearly all cases.

4.5.2. Influence of parameter a in the basis function

The parameter a in the basis function (see (6)) affects the non-linear modeling ability of RBF and, thus, plays an important role in RBF interpolation. This necessitates the analysis of the parameter for the proposed SPM method. The parameter a should take neither too large nor too small values. If a is too large, according to the properties of the Gaussian function, all elements in the matrix Φ will be very close to 1. In this case, Φ will be a singular matrix and (10) will not be uniquely solvable, which will lead to unacceptable SPM results consequently. On the other hand, if a is too small, all elements in Φ will be very close to 0 instead, which will also lead to a singular matrix.

We tested the influence of parameter a with 10 values: 0.1, 0.5, 1, 3, 5, 8, 10, 15, 20 and 30. The three groups of synthetic coarse images degraded with four different scales were used again for testing. Fig. 13a–c shows the sensitivity of the proposed SPM method in relation to a . As shown in the three sub-figures, when a is less than 10, the PCC increases with an increase of a in all 12 cases. When a takes values between 10 and 30, the PCC in each case reaches a stable value.

4.5.3. Influence of window size N

Three window sizes, $N = 3, 5$ and 7, were analyzed for the RBF-based SPM method. For each window size, parameter a with 10 values (i.e., 0.1, 0.5, 1, 3, 5, 8, 10, 15, 20 and 30) were considered and the largest PCC was selected from 10 values for comparison

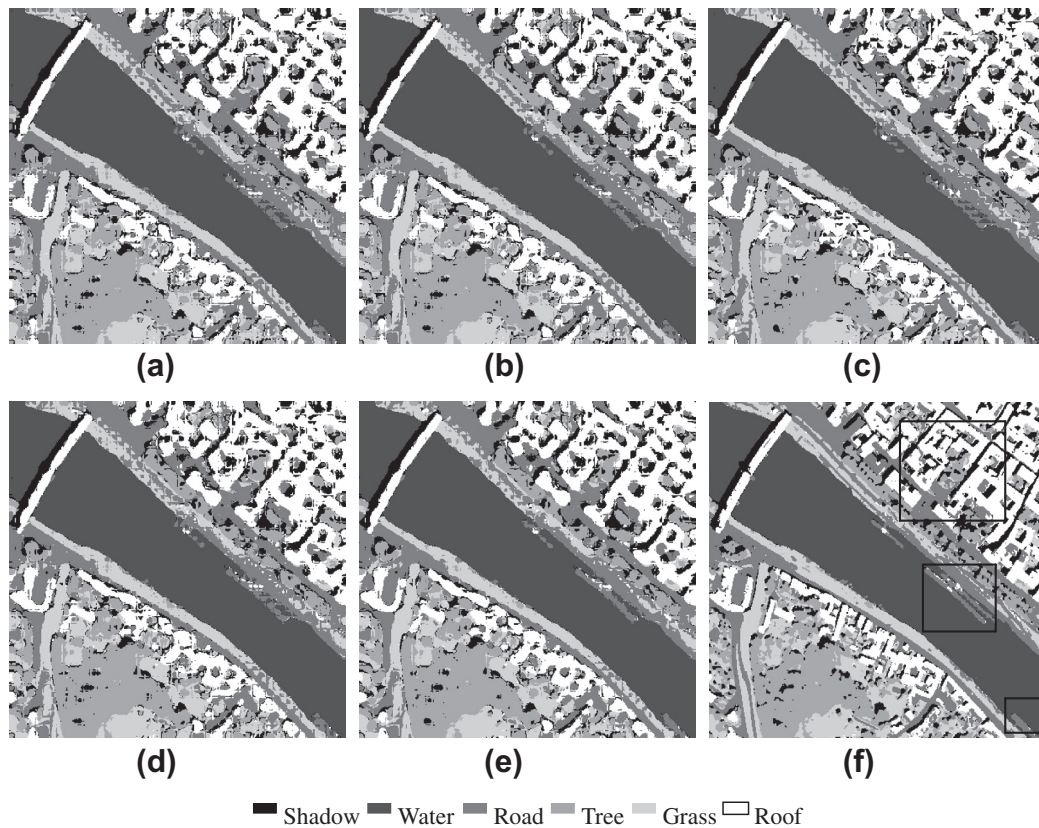


Fig. 8. SPM results of the five methods for the degraded land cover map of the ROSIS image ($S = 8$). (a) Bilinear. (b) Bicubic. (c) SPSAM. (d) Kriging. (e) RBF. (f) Reference with marked areas.

of different window sizes. Fig. 14 shows the PCC for the three window sizes when the three groups of synthetic coarse images degraded with four different scales were tested. It is seen that when N increases from 3 to 5, the PCC increases obviously. When N increases to 7, however, the accuracy gains are relatively limited. In fact, larger N corresponds to larger size of matrix Φ and heavier computing burden in (10). Consequently, $N = 5$ is recommended as a suitable window size for RBF-based SPM, when considering both SPM accuracy and computing efficiency.

5. Discussion

5.1. Computational efficiency

It is important to consider the computing efficiency of SPM methods, especially in real-time applications. The computing time of the five SPM methods at different zoom scales is given in Fig. 15. The time required for the class allocation process (see Section 3.2) was not considered for each SPM method here. On the one hand, this process is very quick (needs less than 3 s in all cases in Fig. 15), which has been demonstrated in Wang et al. (2014a). On the other hand, the class allocation process for all five SPM methods is the same, so can be ignored.

It is seen from the bar charts that the bilinear, bicubic and SPSAM are fast methods whereas the Kriging and RBF methods usually require more time. The geostatistics-based Kriging method considers the spatial covariance in the whole set of prediction data and calculates the contributions from each observed value. For the RBF method ($N = 5$), the model in (10) is built and computed once for each visited mixed pixel. The processes of Kriging and RBF are more complex, thereby, consuming more time than the other three

methods. As learned from Fig. 12 and Table 6 previously, Kriging and RBF are capable of producing greater accuracy than the bilinear, bicubic and SPSAM methods. Therefore, the relatively long running time is the cost of enhancing SPM accuracy for Kriging and RBF. Both the Kriging and RBF methods, however, can still be viewed as real-time algorithms, as they took less than 1 min in the experiments.

Comparing the values in the bar charts in Fig. 15, it is found that for the aerial image with the smallest size among the three tested images, the computing time is the least, whilst for the QuickBird image with the largest size, the time is the most. Therefore, consistent with the other four SPM methods, the computation efficiency of RBF is related to the size of the studied area (i.e., the number of mixed pixels). Furthermore, the computation time of RBF is also a function of the zoom factor.

5.2. Characteristics and advantages of RBF-based SPM

The experimental results shown in Section 4.3–4.5 indicate that the RBF interpolation-based method presented in this paper displays potential for SPM, irrespective of the complexity of land cover pattern in the studied images. In the first experiment, for the SPM of three coarse spatial resolution images with different types of land cover patterns, the new method provides consistently smoother and more continuous SPM results than do the bilinear, bicubic, SPSAM and Kriging methods. The PCC values indicate that the accuracy of the new method is higher than that of the bilinear, bicubic, SPSAM and Kriging methods. When applied to two degraded ROSIS hyperspectral images with different spatial resolutions in the second experiment, where inherent uncertainty exists in soft classification (i.e., LSMA), the new method also produces higher accuracy than the aforementioned four SPM methods.

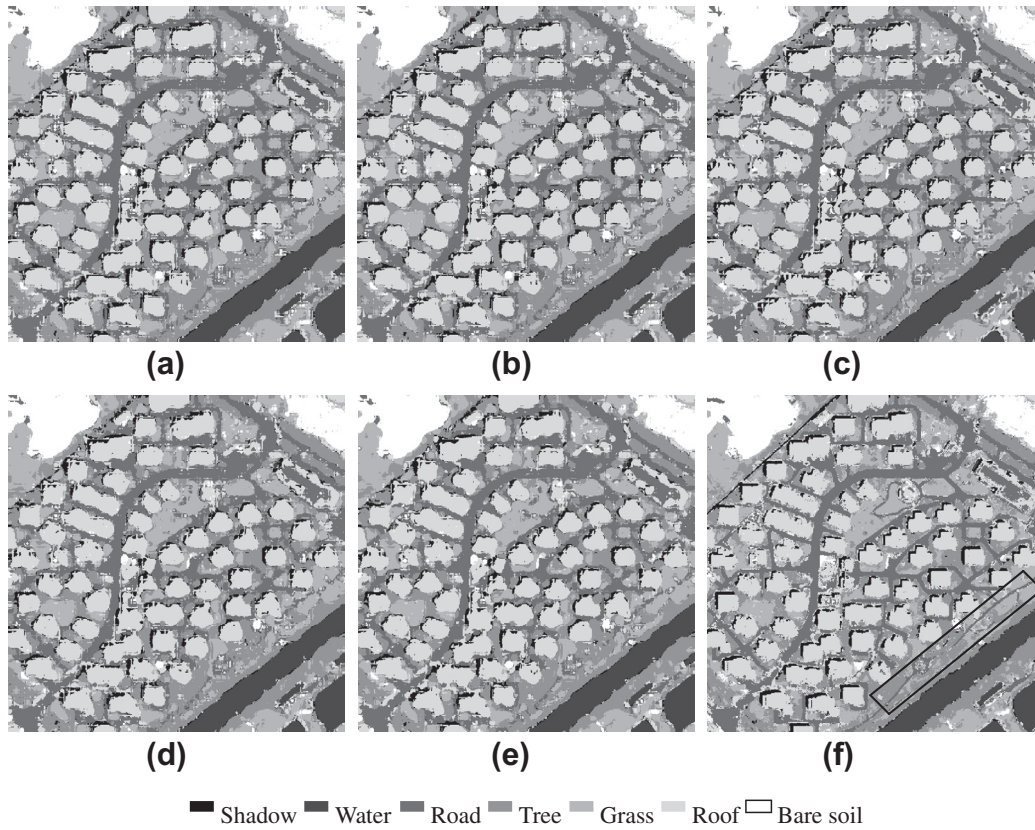


Fig. 9. SPM results of the five methods for the degraded land cover map of the QuickBird image ($S = 8$). (a) Bilinear. (b) Bicubic. (c) SPSAM. (d) Kriging. (e) RBF. (f) Reference with marked area.

Table 2
Accuracy (%) of the HC and five SPM methods for the aerial image.

| | HC | Bilinear | Bicubic | SPSAM | Kriging | RBF |
|-------|-------|----------|---------|-------|--------------|--------------|
| Grass | 76.59 | 92.69 | 92.86 | 92.83 | 93.12 | 93.27 |
| Road | 81.39 | 86.55 | 88.93 | 88.36 | 88.74 | 91.13 |
| River | 80.74 | 95.75 | 95.75 | 95.82 | 96.10 | 95.89 |
| Soil | 83.29 | 91.97 | 91.97 | 92.50 | 92.50 | 92.89 |
| Trees | 72.13 | 89.68 | 90.43 | 90.15 | 90.48 | 91.23 |
| PCC | 76.33 | 91.36 | 91.91 | 91.79 | 92.08 | 92.63 |

Table 3
Accuracy (%) of the HC and five SPM methods for the ROSIS image.

| | HC | Bilinear | Bicubic | SPSAM | Kriging | RBF |
|--------|-------|----------|---------|-------|---------|--------------|
| Shadow | 38.77 | 55.17 | 56.06 | 55.18 | 56.08 | 57.90 |
| Water | 74.76 | 86.14 | 86.11 | 86.24 | 86.46 | 87.29 |
| Road | 67.99 | 72.21 | 72.92 | 73.10 | 73.46 | 74.64 |
| Tree | 75.12 | 74.52 | 75.19 | 74.46 | 75.35 | 75.92 |
| Grass | 65.75 | 70.19 | 71.01 | 71.01 | 71.56 | 72.52 |
| Roof | 80.79 | 80.38 | 80.87 | 80.76 | 81.05 | 81.91 |
| PCC | 68.51 | 72.90 | 73.55 | 73.34 | 73.86 | 74.89 |

The good performance of the proposed method is also further confirmed by the results in Fig. 12, where four different scales were tested for each image.

The advantage of the new method in terms of SPM accuracy can be attributed to the strong non-linear modeling ability of RBF. The core idea of SPM is to either maximize or match prior expectations about spatial dependence. In the proposed method, the spatial autocorrelation between any sub-pixel and its neighboring coarse pixels is characterized by the basis function in RBF interpolation.

Table 4
Accuracy (%) of the HC and five SPM methods for the QuickBird image.

| | HC | Bilinear | Bicubic | SPSAM | Kriging | RBF |
|-----------|-------|----------|--------------|-------|---------|--------------|
| Shadow | 33.18 | 51.67 | 52.51 | 50.92 | 51.80 | 53.34 |
| Water | 83.80 | 91.23 | 91.46 | 91.04 | 90.93 | 91.62 |
| Road | 73.46 | 74.19 | 74.88 | 74.24 | 74.77 | 75.81 |
| Tree | 67.99 | 71.99 | 72.79 | 71.93 | 72.54 | 73.52 |
| Grass | 64.36 | 70.74 | 71.22 | 70.76 | 71.33 | 72.04 |
| Roof | 68.55 | 73.67 | 73.93 | 72.79 | 73.25 | 73.81 |
| Bare soil | 71.09 | 76.55 | 77.11 | 78.17 | 77.28 | 78.04 |
| PCC | 67.16 | 72.10 | 72.67 | 71.88 | 72.38 | 73.24 |

Meanwhile, the spatial autocorrelation between coarse pixels in the input proportion images is exploited fully to adaptively calculate the corresponding coefficients of the basis function values. The proposed SPM method, therefore, tries to capture and use as much of the available information about spatial dependence.

As described systematically in the introduction, for the post-processing of a soft classification, the STHSPM may be considered advantageous in terms of computing efficiency. The proposed SPM algorithm is a newly developed STHSPM algorithm. In all the experiments in this study, the proposed SPM method took less than 1 min for each coarse spatial resolution image. Certainly, the computation time of RBF is related to the size of the studied area and zoom factor. Unlike the back-propagation neural network and Indicator CoKriging, the proposed method does not require any prior class information on spatial structure. With respect to the other two SPM algorithms, SPSAM and Kriging, experimental results suggest that the new method is able to obtain more accurate SPM results. The proposed RBF interpolation-based method, therefore, provides a promising new and real-time SPM method for practical applications.

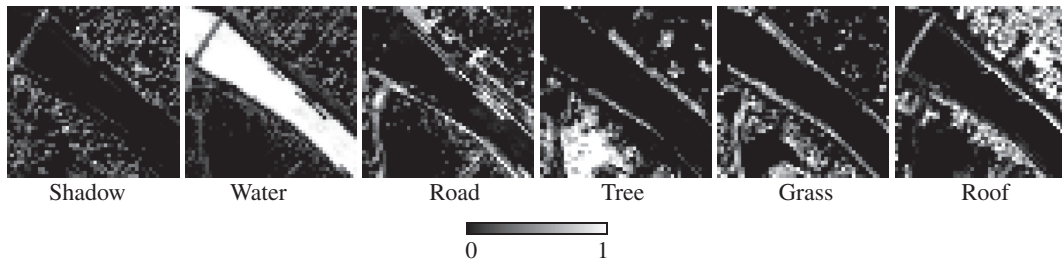


Fig. 10. Proportion images of the 6 classes in the degraded ROSIS hyperspectral image.

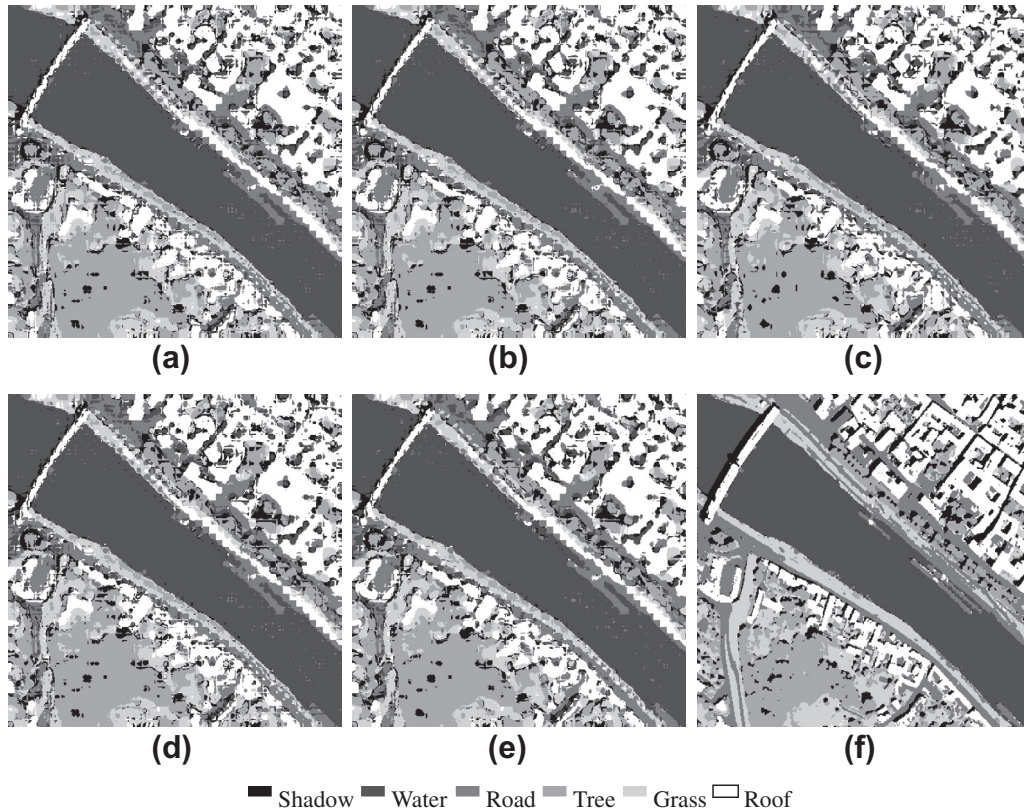


Fig. 11. SPM results of the five methods for the degraded ROSIS hyperspectral image ($S = 8$). (a) Bilinear. (b) Bicubic. (c) SPSAM. (d) Kriging. (e) RBF. (f) Reference.

Table 5
Accuracy (%) of the five SPM methods for the degraded ROSIS hyperspectral images.

| | $S = 4$ | | | | | $S = 8$ | | | | |
|--------|----------|---------|-------|---------|--------------|----------|---------|-------|--------------|--------------|
| | Bilinear | Bicubic | SPSAM | Kriging | RBF | Bilinear | Bicubic | SPSAM | Kriging | RBF |
| Shadow | 49.46 | 49.75 | 50.15 | 50.21 | 50.86 | 33.59 | 34.08 | 34.10 | 34.49 | 35.18 |
| Water | 97.72 | 97.74 | 97.66 | 97.74 | 97.79 | 96.18 | 96.21 | 96.11 | 96.20 | 96.29 |
| Road | 51.96 | 52.37 | 52.70 | 52.91 | 53.23 | 49.41 | 49.64 | 49.50 | 49.83 | 50.11 |
| Tree | 82.33 | 82.50 | 82.33 | 82.54 | 82.62 | 75.45 | 75.87 | 75.89 | 76.14 | 76.44 |
| Grass | 58.21 | 58.45 | 59.10 | 59.04 | 59.13 | 54.71 | 54.87 | 55.62 | 55.68 | 55.56 |
| Roof | 81.35 | 81.54 | 81.28 | 81.35 | 81.68 | 76.66 | 76.90 | 76.46 | 76.63 | 77.20 |
| PCC | 74.48 | 74.67 | 74.76 | 74.86 | 75.08 | 69.80 | 70.02 | 69.99 | 70.18 | 70.45 |

The difference between Kriging and the proposed RBF method is that the former is a global interpolation approach while the latter is a local interpolation strategy. The Kriging method is implemented based on the framework of geostatistical theory which takes the spatial configuration in the entire studied area into consideration and estimates weights for each observed data

point based on the global spatial covariance. The RBF method, however, builds a non-linear model for each coarse pixel, using proportions as well as the locations of its surrounding coarse pixels as observed data. In RBF interpolation, each coarse pixel has its unique set of observed data and RBF interpolation is spatially adaptive.

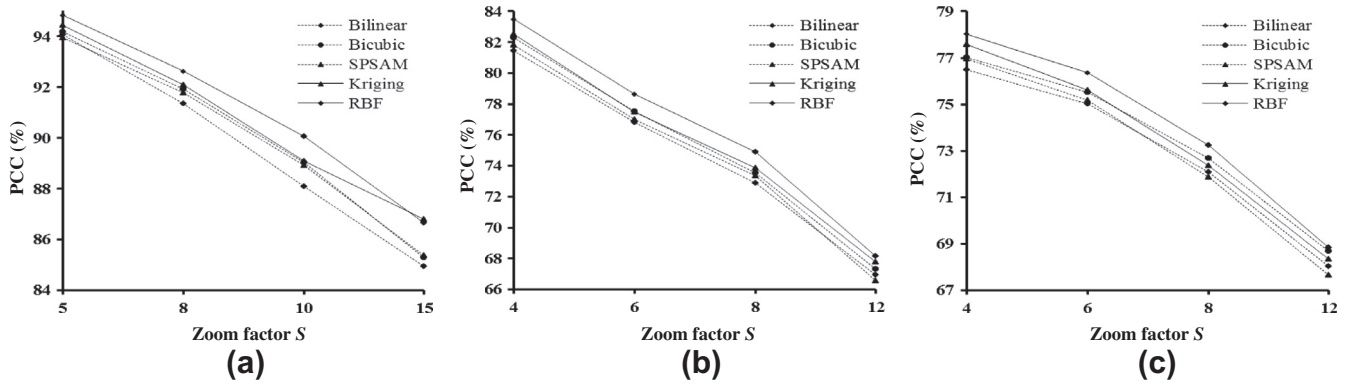


Fig. 12. Performance of the five SPM methods with four different zoom factors. (a) Aerial image. (b) ROSIS image. (c) QuickBird image.

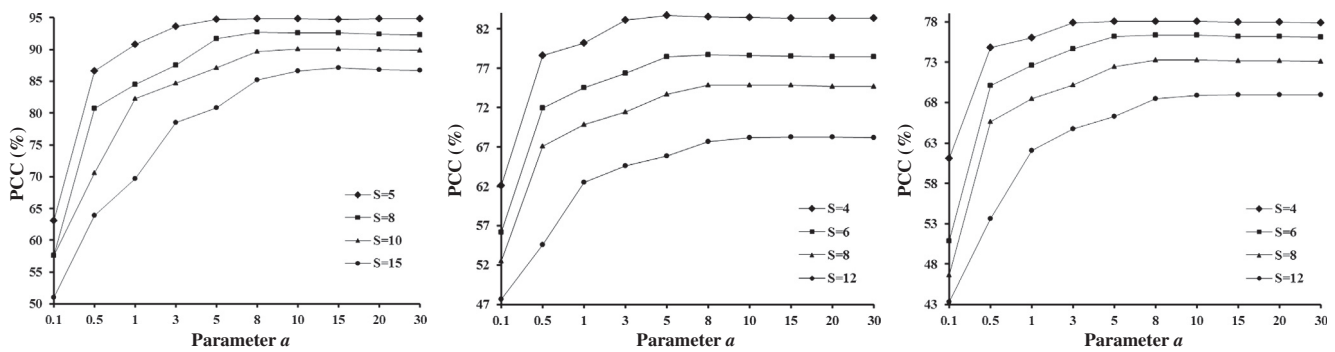


Fig. 13. Influence of parameter a in the basis function of the proposed RBF interpolation-based SPM. (a) Aerial image. (b) ROSIS image. (c) QuickBird image.

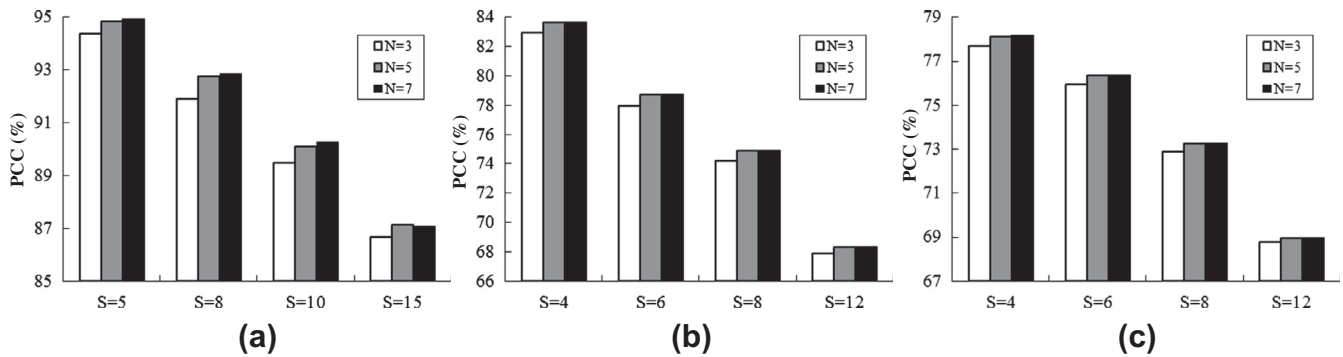


Fig. 14. Influence of the window size in the proposed RBF interpolation-based SPM. (a) Aerial image. (b) ROSIS image. (c) QuickBird image.

5.3. Influences of several factors on RBF-based SPM

Similar to the other SPM methods, the proposed SPM method is sensitive to the zoom scale factor, as shown in Fig. 12. Its accuracy decreases when the zoom factor increases. One main reason is that the SPM problem increases in complexity with larger zoom factors, as for every coarse pixel the locations of more sub-pixels need to be predicted and uncertainty increases. Another reason is that in the coarse images produced with large degraded resolutions, pixels may be larger than some land cover objects, and some objects may fall within isolated coarse pixels. This is referred to as the L-resolution case in Atkinson (2009). In the L-resolution case, the spatial dependence-based SPM methods, including the proposed method, fail to locate objects accurately at fine spatial resolution.

We can observe further from Fig. 12 that the PCC values of the proposed method decreases from Fig. 12a–c. As an example, the

PCC in Fig. 12a is over 94% for $S = 5$, but in Fig. 12b and c for a smaller scale $S = 4$, the PCC declines to be less than 84% and 79%, respectively. This is because from Fig. 12a–c, in the three groups of coarse images, the number of land cover classes increases from five to seven. On the other hand, the complexity of the land cover pattern also increases. From the corresponding three reference maps in Figs. 3b, 4b, and 5b, one can see that the aerial image is occupied by large and continuous objects, which can be well recreated by the new spatial dependence-based SPM method. In the ROSIS and QuickBird images, however, many small objects and elongated features exist, especially in the latter.

Comparing the resulting sub-pixel maps for the ROSIS image in the first experiment to those in the second experiment, it is seen that the errors from soft classification impose a considerably negative effect on the overall accuracy of SPM methods. This can be illustrated by the existence of isolated pixels in Fig. 11a–e, and

Table 6

Comparison between the five SPM methods for the three groups of images with four zoom factors (12 cases in all; A vs. B: + means the PCC of A is higher while - means the PCC of A is smaller).

| | Bicubic | SPSAM | Kriging | RBF |
|----------|---------|--------|---------|--------|
| | vs | vs | vs | vs |
| Bilinear | 12+ | 8+ 4- | 12+ | 12+ |
| Bicubic | | 1+ 11- | 9+ 3- | 12+ |
| SPSAM | | | 12+ | 12+ |
| Kriging | | | | 11+ 1- |
| RBF | | | | |

the fact that some pixels of the shadow class in the reference map in Fig. 11f were incorrectly assigned to the water class in Fig. 11a–e. Regarding the quantitative evaluation of the RBF results for the ROSIS image, the PCC (pure pixels were included for accuracy statistics) reached 91.87% and 81.99% for $S = 4$ and $S = 8$ in the first experiment, where no error exists in soft classification. In the second experiment, however, due to the errors in soft classification, the corresponding PCC decreased by around 17% and 12%, respectively.

As for the parameter a in the basis function, the proposed method tends to obtain highly accurate SPM results when it is set to values between 10 and 30 (see Fig. 13). When a is too large (e.g., 50 in the experiments), it leads to a singular matrix Φ and poor SPM results.

5.4. Change of scale in RBF interpolation

The RBF interpolation is essentially an area-to-point prediction method and its outputs are continuous variables (in SPM these outputs are converted to categories by class allocation in Section 3.2). The challenge with area-to-point prediction is to account explicitly for the change of scale (Atkinson, 2013). More specifically, when predicting the values at an arbitrary sub-pixel (point), the information within any observed coarse pixel (area) needs to be expressed at a finer spatial resolution. This is not the case, however, in RBF interpolation as presented in this paper. RBF interpolation deals with change of scale implicitly: Each observed coarse pixel is treated as a point at its centroid; when the scale factor S changes, the distance calculation in (7) and (8) changes correspondingly, leading to changes of Gaussian function values (see (6)) and matrix Φ (see (12)).

Here, we attempted to consider the change of scale in RBF interpolation in a more explicit way, in which the Gaussian function and matrix Φ are described at the sub-pixel scale

$$\phi(P_n, p_i) = \frac{1}{S^2} \sum_{m=1}^{S^2} e^{-d^2(p_m, p_i)/a^2} \tag{13}$$

$$\phi(P_n, P_v) = \frac{1}{S^4} \sum_{m=1}^{S^2} \sum_{t=1}^{S^2} e^{-d^2(p_m, p_t)/a^2} \tag{14}$$

where p_m denotes any sub-pixel within coarse pixel P_n , p_i denotes any sub-pixel within coarse pixel P_v , $d(p_m, p_i)$ is the distance between the centroid of sub-pixel p_i and the centroid of any sub-pixel p_m within pixel P_n and $d(p_m, p_t)$ is the distance between the centroid of any sub-pixel p_m within P_n and the centroid of any sub-pixel p_t within P_v .

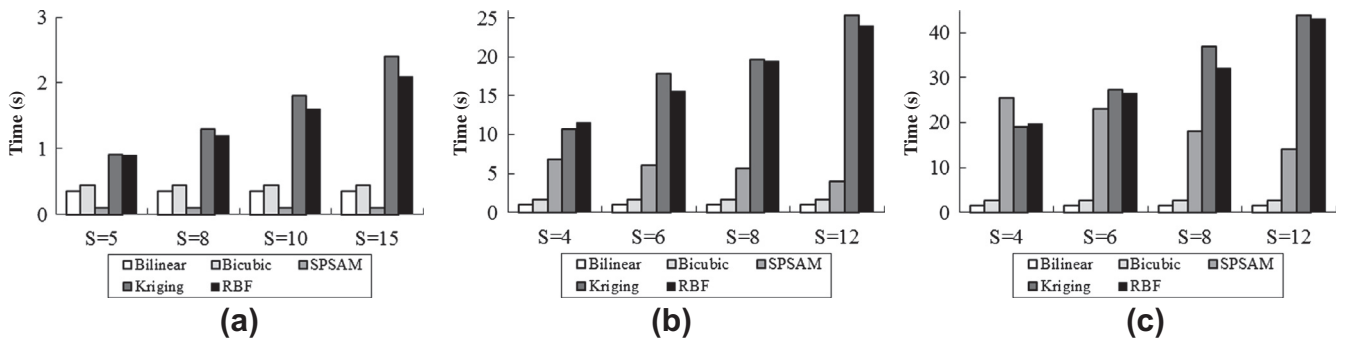


Fig. 15. Computing time (seconds) of the five SPM methods. (a) Aerial image. (b) ROSIS image. (c) QuickBird image.

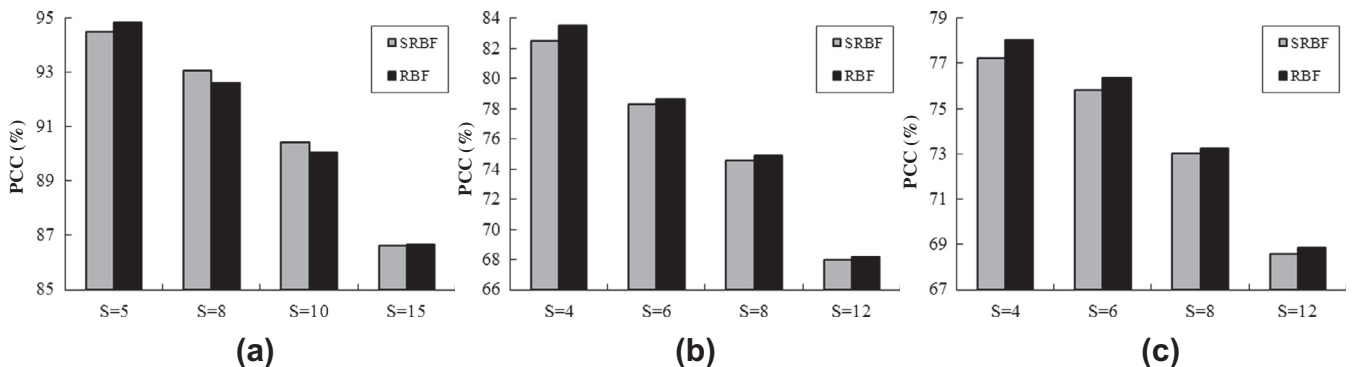


Fig. 16. PCC (%) of the SRBF and RBF-based SPM methods. (a) Aerial image. (b) ROSIS image. (c) QuickBird image.

Table 7
Computing time (seconds) of the SRBF and RBF-based SPM methods.

| | Aerial image | | | | ROSIS image | | | | QuickBird image | | | |
|------|--------------|-------|--------|--------|-------------|-------|-------|--------|-----------------|-------|-------|--------|
| | S = 5 | S = 8 | S = 10 | S = 15 | S = 4 | S = 6 | S = 8 | S = 12 | S = 4 | S = 6 | S = 8 | S = 12 |
| SRBF | 2.2 | 10 | 22.8 | 110.7 | 12.3 | 18.3 | 28.5 | 69.0 | 20.6 | 29.7 | 42.0 | 86.6 |
| RBF | 0.9 | 1.4 | 1.6 | 2.1 | 11.6 | 15.6 | 19.5 | 24.0 | 19.7 | 26.6 | 32.0 | 43.0 |

A question is whether the scheme in (13) and (14) will impart benefits for RBF interpolation. For simplicity, we denote the revised RBF that considers the change of scale with (13) and (14) as SRBF. The two interpolation algorithms, SRBF and RBF, were tested and compared using the three remote sensing images, with four scale factors for each image. The PCC of the SRBF and RBF-based SPM is shown in Fig. 16. Values in the three bar charts indicate SRBF does not increase the accuracy of SPM. This suggests that SRBF will decrease the non-linear modeling ability of the original RBF. The computational burden of two versions of interpolation algorithms is exhibited in Table 7. Again, the time needed in class allocation is not taken into consideration. It is demonstrated that SRBF needs more computing time than RBF for the task of interpolation, due to the more complicated calculation process in (13) and (14). Consequently, SRBF is not an advisable scheme for RBF.

5.5. Future work

Due to the diversity of land cover distributions in the real world, the SPM problem is usually under-determined, with multiple plausible solutions such that many sub-pixel land cover maps can lead to an equally coherent recreation of the input coarse image (Boucher and Kyriakidis, 2006). The inherent uncertainty in the SPM problem limits the accuracy of the proposed SPM method, especially in large scale cases. The additional information from auxiliary data can be useful in addressing the under-determined problem. In recent years, various auxiliary information has been applied to enhance SPM, such as LIDAR data (Nguyen et al., 2005), sub-pixel shifted remote sensing images (Wang and Wang, 2013; Xu et al., 2013; Wang et al., 2014b; Wang and Shi, 2014) (in some cases from time-series imagery (Shao and Lunetta, 2011; Muad and Foody, 2012b)), panchromatic images (Ardila et al., 2011; Nguyen et al., 2011; Li et al., 2013), high resolution color images (Mahmood et al., 2013) and shape information (Ling et al., 2012b; Thornton et al., 2007). It is expected that such auxiliary information will enable further improvement of the proposed RBF interpolation-based SPM method, particularly for reproduction of elongated features and small objects in the L-resolution case. Designing the appropriate way to incorporate the supplementary information to the RBF-based SPM model would be an interesting challenge for the future.

As mentioned in the introduction, there are relations between SPM and super-resolution reconstruction. The RBF interpolation presented in this paper can also be employed for the purpose of super-resolution reconstruction, taking the coarse spatial resolution remote sensing images in units of reflectance as input. The output of RBF interpolation will be the desired multispectral or hyperspectral remote sensing image at a fine spatial resolution, which can then be classified by a hard classifier to generate fine spatial resolution land cover maps. Our future research will focus on this.

6. Conclusion

This paper presents a new RBF interpolation-based SPM method for remote sensing images. The new method first utilizes RBF interpolation to predict the soft class values at each sub-pixel. Under

the coherence constraint imposed by the coarse resolution land cover proportions, a sub-pixel map is then generated by hardening the soft class values. Based on the non-linear modeling ability of the RBF, the proposed method makes full use of the available spatial information to characterize spatial dependence, and does not need any prior information. The new method is also free of iteration and involves few parameters. Both visual and quantitative assessment on a range of experimental results reveals that the proposed method provides greater accuracy in comparison with bilinear-, bicubic-, SPSAM- and Kriging-based SPM methods. Moreover, the performance of the proposed SPM method is related to the quality of soft classification, the zoom factor, the number of classes required and the spatial complexity of the land cover pattern in the studied image. Future research will focus on making use of auxiliary variables to enhance the proposed SPM method and applying RBF interpolation directly to multispectral or hyperspectral remote sensing image for sub-pixel land cover mapping.

Acknowledgements

The authors would like to thank Dr. Andrew J. Tatem of the University of Southampton for providing the land cover map in Bristol, UK, Dr. Lefeiz Zhang of Wuhan University for providing the land cover maps of ROSIS, Dr. Hua Zhang from the China University of Mining and Technology, Xuzhou, China, for providing the Xuzhou QuickBird image and the land cover map, and Prof. Paolo Gamba of the University of Pavia for providing the ROSIS data used in this paper. The authors would also like to thank the handling editor Prof. Civco and anonymous reviewers for their valuable comments and suggestions. This work was supported by the Ministry of Science and Technology of China under Project 2012BAJ15B04 and Project 2012AA12A305.

References

- Ardila, J.P., Tolpekin, V.A., Bijker, W., Stein, A., 2011. Markov-random-field-based super-resolution mapping for identification of urban trees in VHR images. *ISPRS J. Photogram. Remote Sens.* 66, 762–775.
- Atkinson, P.M., 1997. Mapping sub-pixel boundaries from remotely sensed images. *Innov. GIS* 4, 166–180.
- Atkinson, P.M., 2005. Sub-pixel target mapping from soft-classified, remotely sensed imagery. *Photogram. Eng. Remote Sens.* 71 (7), 839–846.
- Atkinson, P.M., 2009. Issues of uncertainty in super-resolution mapping and their implications for the design of an inter-comparison study. *Int. J. Remote Sens.* 30 (20), 5293–5308.
- Atkinson, P.M., 2013. Downscaling in remote sensing. *Int. J. Appl. Earth Obs. Geoinf.* 22, 106–114.
- Bioucas-Dias, J.M., Plaza, A., Dobigeon, N., Parente, M., Du, Q., Gader, P., Chanussot, J., 2012. Hyperspectral unmixing overview: geometrical, statistical and sparse regression-based approaches. *IEEE J. Selected Topics Appl. Earth Observ. Remote Sens.* 5 (2), 354–379.
- Boucher, A., Kyriakidis, P.C., 2006. Super-resolution land cover mapping with indicator geostatistics. *Remote Sens. Environ.* 104 (3), 264–282.
- Buhmann, M.D., 2003. *Radial Basis Functions: Theory and Implementations*. Cambridge University Press, Cambridge, UK.
- Carr, J.C., Fright, W.R., Beatson, R.K., 1997. Surface interpolation with radial basis functions for medical imaging. *IEEE Trans. Med. Imag* 16 (1), 96–107.
- Carr, J.C., Beatson, R.K., Cherrie, J.B., Mitchell, T.J., Fright, W.R., McCallum, B.C., Evans, T.R., 2001. Reconstruction and representation of 3D objects with radial basis functions. In: *Proceedings of the 28th Annual Conference on Computer Graphics and Interactive Techniques*, pp. 67–76.
- Foody, G.M., 2000. Estimation of sub-pixel land cover composition in the presence of untrained classes. *Comput. Geosci.* 26, 469–478.

- Foody, G.M., Muslim, A.M., Atkinson, P.M., 2005. Super-resolution mapping of the waterline from remotely sensed data. *Int. J. Remote Sens.* 26 (24), 5381–5392.
- Fuji, Y., Abe, Y., Iiguni, Y., 2012. Matching parameter estimation by using the radial basis function interpolation. *IET Image Proc.* 6 (4), 407–416.
- Ge, Y., 2013. Sub-pixel land-cover mapping with improved proportion images upon multiple-point simulation. *Int. J. Appl. Earth Obs. Geoinf.* 22, 115–126.
- González, J., Rojas, I., Ortega, J., Pomares, H., Fernández, F.J., Díaz, A.F., 2003. Multiobjective evolutionary optimization of the size, shape, and position parameters of radial basis function networks for function approximation. *IEEE Trans. Neural Networks* 14 (6), 1478–1495.
- Heinz, D.C., Chang, C.-I., 2001. Fully constrained least squares linear spectral mixture analysis method for material quantification in hyperspectral imagery. *IEEE Trans. Geosci. Remote Sens.* 39 (3), 529–545.
- Jin, H., Mountrakis, G., Li, P., 2012. A super-resolution mapping method using local indicator variograms. *Int. J. Remote Sens.* 33 (24), 7747–7773.
- Kasetkasem, T., Arora, M.K., Varshney, P.K., 2005. Super-resolution land-cover mapping using a Markov random field based approach. *Remote Sens. Environ.* 96 (3/4), 302–314.
- Lee, Y.J., Yoon, J., 2010. Nonlinear image upsampling method based on radial basis function interpolation. *IEEE Trans. Image Process.* 19 (10), 2682–2692.
- Li, F., Jia, X., Fraser, D., 2009. Superresolution reconstruction of multispectral data for improved image classification. *IEEE Geosci. Remote Sens. Lett.* 6 (4), 689–693.
- Li, X., Ling, F., Du, Y., Zhang, Y., 2013. Spatially adaptive superresolution land cover mapping with multispectral and panchromatic images. *IEEE Trans. Geosci. Remote Sens.* <http://dx.doi.org/10.1109/TGRS.2013.2266345>.
- Ling, F., Du, Y., Xiao, F., Li, X., 2012a. Subpixel land cover mapping by integrating spectral and spatial information of remotely sensed imagery. *IEEE Geosci. Remote Sens. Lett.* 9 (3), 408–412.
- Ling, F., Li, X., Xiao, F., Fang, S., Du, Y., 2012b. Object-based sub-pixel mapping of buildings incorporating the prior shape information from remotely sensed imagery. *Int. J. Appl. Earth Obs. Geoinf.* 18, 283–292.
- Magoules, F., Diago, L.A., Hagiwara, I., 2007. Efficient preconditioning for image reconstruction with radial basis functions. *Adv. Eng. Softw.* 38, 320–327.
- Mahmood, Z., Akhter, M.A., Thoonen, G., Scheunders, P., 2013. Contextual subpixel mapping of hyperspectral images making use of a high resolution color image. *IEEE J. Select. Topics Appl. Earth Observ. Remote Sens.* 6 (2), 779–791.
- Makido, Y., Shortridge, A., Messina, J.P., 2007. Assessing alternatives for modeling the spatial distribution of multiple land-cover classes at sub-pixel scales. *Photogram. Eng. Remote Sens.* 73 (8), 935–943.
- Mertens, K.C., Verbeke, L.P.C., Ducheyne, E.I., De Wulf, R., 2003. Using genetic algorithms in sub-pixel mapping. *Int. J. Remote Sens.* 24 (21), 4241–4247.
- Mertens, K.C., Basets, B.D., Verbeke, L.P.C., De Wulf, R., 2006. A sub-pixel mapping algorithm based on sub-pixel/pixel spatial attraction models. *Int. J. Remote Sens.* 27 (15), 3293–3310.
- Muad, A.M., Foody, G.M., 2012a. Impact of land cover patch size on the accuracy of patch area representation in HNN-based super resolution mapping. *IEEE J. Selected Topics Appl. Earth Observ. Remote Sens.* 5 (5), 1418–1427.
- Muad, A.M., Foody, G.M., 2012b. Super-resolution mapping of lakes from imagery with a coarse spatial and fine temporal resolution. *Int. J. Appl. Earth Obs. Geoinf.* 15, 79–91.
- Nguyen, M.Q., Atkinson, P.M., Lewis, H.G., 2005. Superresolution mapping using a Hopfield neural network with LIDAR data. *IEEE Geosci. Remote Sens. Lett.* 2 (3), 366–370.
- Nguyen, M.Q., Atkinson, P.M., Lewis, H.G., 2011. Super-resolution mapping using Hopfield neural network with panchromatic imagery. *Int. J. Remote Sens.* 32 (21), 6149–6176.
- Nigusse, D., Zurita-Milla, R., Clevers, J.G.P.W., 2011. Possibilities and limitations of artificial neural networks for subpixel mapping of land cover. *Int. J. Remote Sens.* 32 (22), 7203–7226.
- Pollandt, R., 1997. Solving nonlinear differential equations of mechanics with the boundary element method and radial basis functions. *Int. J. Numer. Meth. Eng.* 40 (1), 61–73.
- Shao, Y., Lunetta, R.S., 2011. Sub-pixel mapping of tree canopy, impervious surfaces, and cropland in the Laurentian Great Lakes basin using MODIS time-series data. *IEEE J. Selected Topics Appl. Earth Observ. Remote Sens.* 4 (2), 336–347.
- Su, Y.F., Foody, G.M., Muad, A.M., Cheng, K.S., 2012. Combining pixel swapping and contouring methods to enhance super-resolution mapping. *IEEE J. Selected Topics Appl. Earth Observ. Remote Sens.* 5 (5), 1428–1437.
- Tatem, A.J., 2002. Super-Resolution Land Cover Mapping from Remotely Sensed Imagery Using a Hopfield Neural Network. Ph.D. Dissertation, University of Southampton.
- Tatem, A.J., Lewis, H.G., Atkinson, P.M., Nixon, M.S., 2001. Multi-class land cover mapping at the sub-pixel scale using a Hopfield neural network. *Int. J. Appl. Earth Obs. Geoinf.* 3 (2), 184–190.
- Thornton, M.W., Atkinson, P.M., Holland, D.A., 2007. A linearised pixel-swapping method for mapping rural linear land cover features from fine spatial resolution remotely sensed imagery. *Comput. Geosci.* 33, 1261–1272.
- Tolpekin, V.A., Stein, A., 2009. Quantification of the effects of land-cover-class spectral separability on the accuracy of Markov-random-field based superresolution mapping. *IEEE Trans. Geosci. Remote Sens.* 47 (9), 3283–3297.
- Torres, C.E., Barba, L.A., 2009. Fast radial basis function interpolation with Gaussians by localization and iteration. *J. Comput. Phys.* 228, 4976–4999.
- Verhoeve, J., Wulf, R.De., 2002. Land-cover mapping at sub-pixel scales using linear optimization techniques. *Remote Sens. Environ.* 79 (1), 96–104.
- Villa, A., Chanussot, J., Benediktsson, J.A., Jutten, C., 2011. Spectral unmixing for the classification of hyperspectral images at a finer spatial resolution. *IEEE J. Selected Topics Signal Process.* 5 (3), 521–533.
- Wang, Q., Shi, W., 2014. Utilizing multiple subpixel shifted image in subpixel mapping with image interpolation. *IEEE Geosci. Remote Sens. Lett.* 11 (4), 798–802.
- Wang, L., Wang, Q., 2013. Subpixel mapping using Markov random field with multiple spectral constraints from subpixel shifted remote sensing images. *IEEE Geosci. Remote Sens. Lett.* 10 (3), 598–602.
- Wang, S., Lim, K., Khoo, B., Wang, M., 2007. An extended level set method for shape and topology optimization. *J. Comput. Phys.* 221 (1), 395–421.
- Wang, Q., Wang, L., Liu, D., 2012. Particle swarm optimization-based sub-pixel mapping for remote-sensing imagery. *Int. J. Remote Sens.* 33 (20), 6480–6496.
- Wang, Q., Shi, W., Wang, L., 2014a. Allocating classes for soft-then-hard subpixel mapping algorithms in units of class. *IEEE Trans. Geosci. Remote Sens.* 52 (5), 2940–2959.
- Wang, Q., Shi, W., Wang, L., 2014b. Indicator cokriging-based subpixel land cover mapping with shifted images. *IEEE J. Selected Topics Appl. Earth Observ. Remote Sens.* 7 (1), 327–339.
- Xu, X., Zhong, Y., Zhang, L., Zhang, H., 2013. Sub-pixel mapping based on a MAP model with multiple shifted hyperspectral imagery. *IEEE J. Selected Topics Appl. Earth Observ. Remote Sens.* 6 (2), 580–593.
- Zhang, L., Zhang, L., Tao, D., Huang, X., 2013. Tensor discriminative locality alignment for hyperspectral image spectral-spatial feature extraction. *IEEE Trans. Geosci. Remote Sens.* 51 (1), 242–256.
- Zhong, Y., Zhang, L., 2012. Remote sensing image subpixel mapping based on adaptive differential evolution. *IEEE Trans. Systems, Man, and Cybern. – Part B: Cybern.* 42 (5), 1306–1329.